PROCEEDINGS, 44th Workshop on Geothermal Reservoir Engineering
Stanford University, Stanford, California, February 11-13, 2019
SGP-TR-214

Flow Path of Injected Water Inferred from Microseismic Monitoring in the Okuaizu Geothermal Field, Japan

Kyosuke Okamoto, Hiroshi Asanuma, Takashi Okabe, Yasuyuki Abe, Masatoshi Tsuzuki

2-2-9, Machiikedai, Koriyama, Fukushima 963-0298, Japan

okamoto.kyosuke@aist.go.jp

Keywords: Microseismic monitoring, Seismology, Water injection, Flow path

ABSTRACT

A continuous water injection test was conducted to halt the reduction of steam production in the Okuaizu Geothermal Field, Japan. One of the possible effects associated with water flows is creation of tensile seismic events. Those events are likely triggered by inflow into or outflow from fractures in a rock body. In this study, the tensile seismic events were employed as a proxy of water flows. We conducted a focal mechanism inversion considering tensile angle in addition to strike, dip and rake angles, which are used in conventional inversions. Hypocenters of seismic events were determined by a cluster analysis (double-difference method) and the focal parameters were determined by a genetic algorithm. The result showed that seismic events with positive tensile angle, which inferred inflow into fractures, are mainly appeared around the injection point and gradually evolved toward a northwest part of the injection point. It suggests that the injected water may flow toward the northwest direction. Meanwhile, our past research pointed out that a high-permeable zone may exist between the injection point and the northwest part. The result of the focal mechanism inversion supports the existence of the fracture zone. We concluded that the focal mechanism analysis considering tensile angle is one of the powerful tools to estimate water flows in subsurface.

1. INTRODUCTION

During water injection into geothermal reservoirs, it is important to monitor and control migration of the fluid to avoid cooling of the reservoir and to retrieve steam efficiently. For this purpose, microseismic monitoring has been widely used to estimate the spatiotemporal behavior of reservoirs (e.g., Fehler et al., 1987; Baria et al., 1999). In the Okuaizu Geothermal Field, Japan, a water injection test has been conducted since 2015. We conducted a high-resolution hypocenter determination using the double-difference (DD, Waldhauser and Ellsworth, 2000) method to understand the behavior of the injected water (Okamoto et al., 2018). In this study, we analyzed focal mechanisms of seismic events during the injection test considering non-double couple (non-DC) components, which are associated with water inflow into and outflow from rock fractures (Vavryčuk and Hrubcová, 2017).

Using the result as a proxy of water flow, we evaluate the relationship between the location of hypocenters and the water flow. Mainly in this study, we focus on the methodology of the focal mechanism analysis to estimate water flow. We show a simple result of the estimated water flow in the Okuaizu Geothermal Field.

2. OUTLINE OF THE INJHECTION TEST AND MICROSEISMIC MONITORING

As part of the "Technology to Evaluate and Manage Geothermal Reservoirs" project conducted by the Japan Oil, Gas and Metals National Corporation (JOGMEC) (e.g., Okabe et al., 2016), a continuous water injection (without pressurization; the average wellhead pressure during injection was 0.17 MPa) test was conducted in the Okuaizu Geothermal Field, Fukushima, Japan (Figure 1), from June to August 2015 in an effort to stop the reduction of steam production. The total amount of injected fluid was approximately 1.2×10^5 m^3. During the initial stage of the test (days 0 to 60), the injection rate was 50 m^3/h (1.39×10^{-2} m^3/s); in the final stage (day 60 to the end of injection), the rate was 70 m^3/h (1.94×10^{-2} m^3/s) (see Figure 2). A step rate test had been conducted for roughly 10 days from the start of injection before the injection rate was stabilized to 50 m^3/h. Figure 1 shows the injection well—called the Test Well in this study—and the injection points, which are indicated by the green line and blue circles, respectively. The injection target area was a heating zone in the geothermal field.

Five stations on the surface and four stations in boreholes (shown in Figure 1) have been deployed around the Test Well since 2015 as part of the project. These stations possess three-component broadband accelerometers or velocimeters. Continuous seismic records are transmitted to a National Institute of Advanced Industrial Science and Technology server in real time, and hypocenters are routinely determined by manual selection of P-wave arrivals. The residuals in P-wave travel times for the estimated hypocenters are, at most, 100 ms (~10^2-m error in the spatial domain). The lower limit of the detectable local seismic magnitude is approximately -2.0. During the injection test, roughly 1,000 microseismic events were detected.

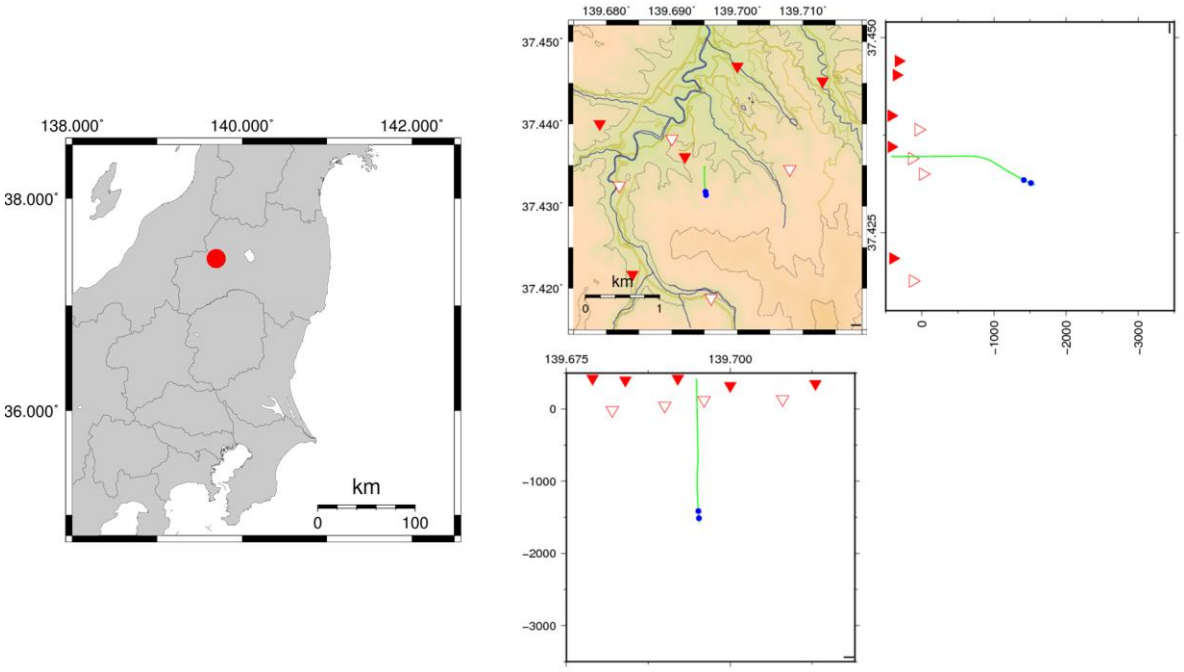

Figure 1: (Left) Location of the Okuaizu Geothermal Field. (Right) Geometry for the injection well (the green line with the injection point shown by the blue circle) and seismic stations (borehole sensor: white triangle, sensor on the surface: red triangle).

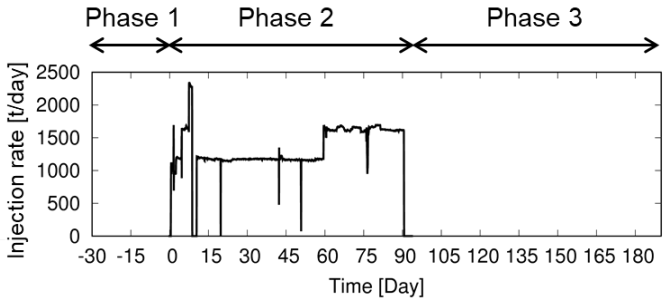

Figure 2: Injection rate of water. The horizontal axis shows the number of days from the start of injection;

3. HIGH-RESOLUTION HYPOCENTER DETERMINATION

We employed cluster analysis of microseismic events to determine the precise locations of the events associated with the injection test. The analysis was applied over three periods (see Figure. 2): (1) for one month before the start of injection (Phase 1), (2) for three months during injection (Phase 2), and (3) for three months after the injection ended (Phase 3). Clusters of microseismic events were identified by cross-correlation of the waveforms (e.g., Schaff et al., 2004) of the up-down (UD) component in the 40–80 Hz frequency range of sensors. The relative difference in the time of arrival of the P-waves in a cluster was calculated on the basis of the cross-correlation to create the input for the DD method. The spatial residuals were on the order of 10^1 m after the hypocenters were relocated; the centroid of a cluster was that for routine hypocenter determination.

The microseismicity that occurred in Phase 1 in an area northeast of the Test Well (see Figure 3a) is considered to be on an existing fault (the geometry of the fault is as specified in New Energy Development Organization, 1997). Two seismic clouds (Mqs1 and 2; see Figure 3b) were seen in Phase 2. The microseismic events in Mqs1 occurred near the injection point in the initial stage of Phase 2 and subsequently spread toward a shallower part. Mqs2 likely occurred on the existing fault on which the microseismic events were concentrated in Phase 1. In Phase 3, the seismicity of Mqs1 and 2 became low, and Mqs3 occurred in an area northwest of the Test Well (see Figure 3c).

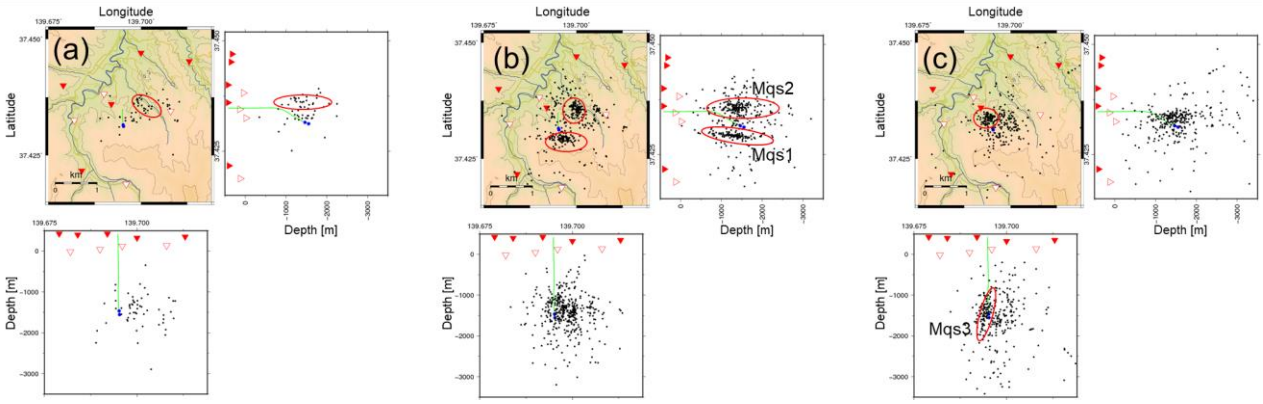

Figure 3: Hypocenter maps for (a) before the start of injection (Phase 1), (b) during injection (Phase 2), and (c) after the end of injection (Phase 3). The red and white triangles mark seismic stations on and below the surface, respectively.

4. FOCAL MECHANISM ANALYSYS

4.1 Method

We estimated focal mechanisms of the seismic events determined by the DD method. In the estimation, polarity of P-wave arrivals and the ratio between P- and S-wave amplitudes (*PS*) were used for the objective function (Eq. 1). In general, amplitude of observed seismic waves are likely different from theoretical one due to inhomogeneities in velocity structures along wave path, resulting in distortion of the estimated moment tensors. In this study, we tried to reduce the effect of distortion by using ratio of P- and S-wave amplitudes.

$$\min_{\mathbf{m}} \left[\frac{\sum_{i=1}^{N} \left(PS_i^{Theo.} - PS_i^{Obs.} \right)^2}{\sum_{i=1}^{N} \left(PS_i^{Obs.} \right)^2} + \alpha \frac{\sum_{i=1}^{N} Pol_i}{N} \right] \tag{1},$$

where **m** is the model parameter, α is the hyper parameter and N is the number of the stations. In this study, we set α to 2. The superscript *Obs.* and *Theo.* represent the values from observation and theoretical calculation, respectively. *Pol* is the number of the stations where the observed and theoretical polarities do not coincide with each other. The theoretical P- and S-wave amplitudes (R_P, $R_S = (R_{SV}^2+R_{SH}^2)^{0.5}$) are calculated according to Eqs. 2-4 (they are reprinted from Ou 2008; Kwiatek and Ben-Zion 2013). These amplitudes were determined in the frequency domain assuming the omega-square low (Aki, 1967) for the source.

$$R_P = \mathbf{r}^T \mathbf{S} \mathbf{r} \tag{2},$$

$$R_{SV} = \mathbf{\Theta}^T \mathbf{S} \mathbf{r} \tag{3},$$

$$R_{SH} = \mathbf{\Phi}^T \mathbf{S} \mathbf{r} \tag{4},$$

where $\mathbf{r} = \sin\theta\cos\phi\,\mathbf{e_1} + \sin\theta\sin\phi\,\mathbf{e_2} + \cos\theta\,\mathbf{e_3}$, $\mathbf{\Theta} = \cos\theta\cos\phi\,\mathbf{e_1} + \cos\theta\sin\phi\,\mathbf{e_2} - \sin\theta\,\mathbf{e_3}$ and $\mathbf{\Phi} = -\sin\phi\,\mathbf{e_1} + \cos\phi\,\mathbf{e_2}$ (ϕ and θ are azimuth and take-off angle, and $\mathbf{e}_i$ is the unit vectors for the i-th direction). The components of **S** are defined by Eqs. 5-10 (from Ou 2008; Kwiatek and Ben-Zion 2013).

$$S_{11} = \left(\frac{2\sigma}{1-2\sigma} + 2\sin^2\delta\sin^2\varphi \right)\sin\gamma - \left(\sin\delta\cos\lambda\sin 2\varphi + \sin 2\delta\sin\lambda\cos^2\varphi \right)\cos\gamma \tag{5},$$

$$S_{22} = \left(\frac{2\sigma}{1-2\sigma} + 2\sin^2\delta\sin^2\varphi \right)\sin\gamma + \left(\sin\delta\cos\lambda\sin 2\varphi - \sin 2\delta\sin\lambda\cos^2\varphi \right)\cos\gamma \tag{6},$$

$$S_{33} = \left(\frac{2\sigma}{1-2\sigma} + 2\cos^2\delta \right)\sin\gamma + \sin 2\delta\sin\lambda\cos\gamma \tag{7},$$

$$S_{12} = -\sin^2\delta \sin 2\varphi \sin\gamma + \left(\sin\delta\cos\lambda\cos 2\varphi + \sin 2\delta \sin\lambda \sin 2\varphi/2\right)\cos\gamma \quad (8),$$

$$S_{13} = \sin 2\delta \sin\varphi \sin\gamma - \left(\cos\delta\cos\lambda\cos\varphi + \cos 2\delta \sin\lambda\sin\varphi\right)\cos\gamma \quad (9),$$

$$S_{23} = -\sin 2\delta \cos\varphi \sin\gamma - \left(\cos\delta\cos\lambda\sin\varphi - \cos 2\delta \sin\lambda\sin\varphi\right)\cos\gamma \quad (10),$$

where σ is the Poisson's ratio (set to 0.25), φ, δ, λ and γ are strike, dip, rake and tensile angles, respectively. The azimuth and take-off angle are determined from the result of hypocenter determination. The remaining parameters to be determined are strike, dip, rake and tensile angles. We determined these parameters by using a genetic algorithm (GA). In general, a priori information (e.g., direction of strike) may help to restrict the possible focal mechanisms and stabilize the solution. However, in the Okuaizu Geothermal Field, there seems to be several major fractures having different strike directions. Therefore, it is difficult to give a priori strike direction to the GA. We repeated the GA algorithms 100 times changing the initial seed for the GA and selected the most frequent solution.

4.2 Application to the field data

We applied the focal mechanism analysis to the seismic events with the local magnitude (approximately > 1) occurred during the injection test. Figure 4 shows the estimated focal mechanisms in Phase1, 2 and 3. The numbers of the analyzed earthquakes in Phase 1, 2 and 3 were 3, 14 and 12, respectively. From those mechanisms, we extracted the information of tensile angle, which has a relationship with subsurface water flows (Figure 5).

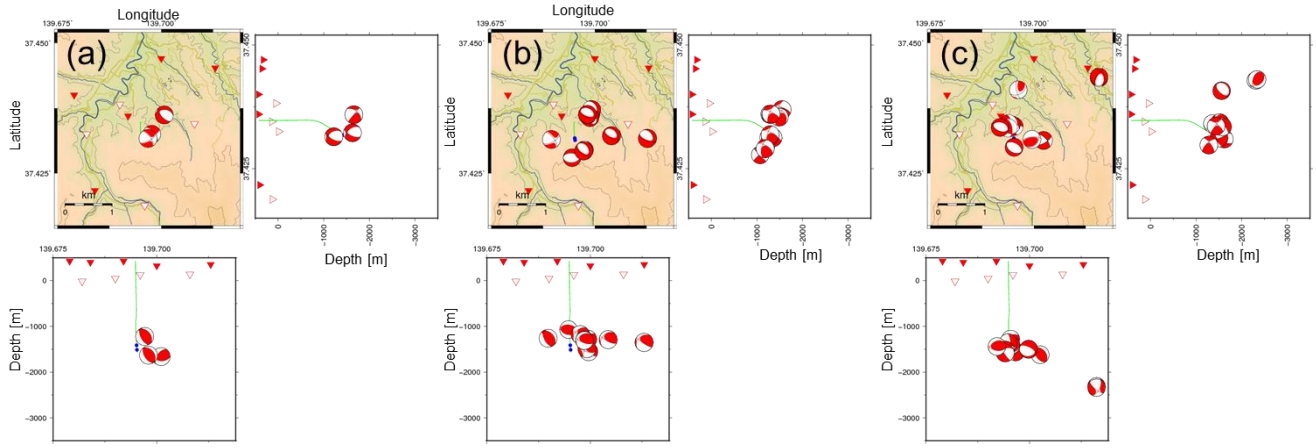

Figure 4: Distribution of fault plane mechanism for (a) Phase 1, (b) Phase 2 and (c) Phase 3.

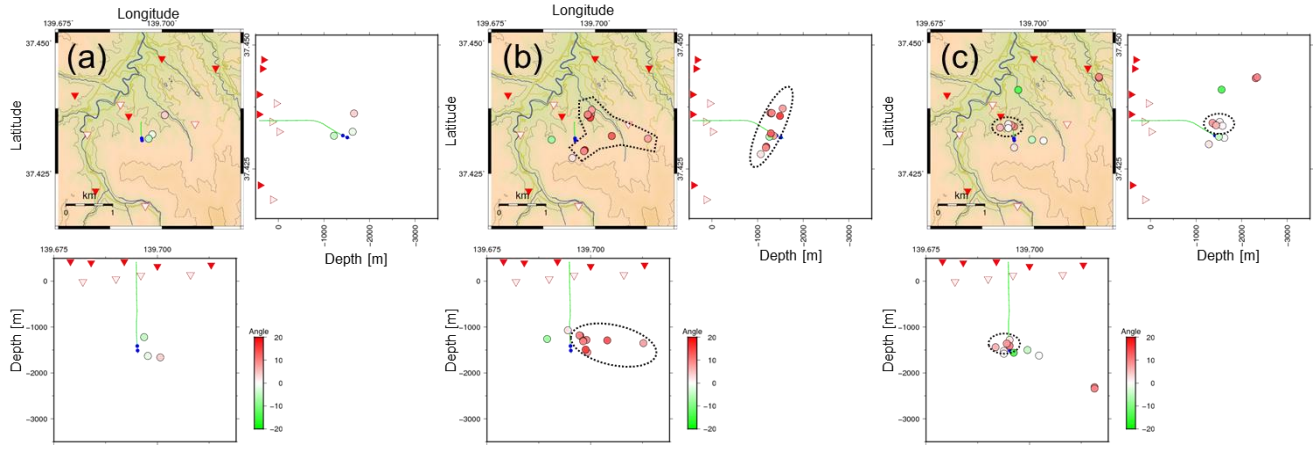

Figure 5: Distribution of tensile angle for (a) Phase 1, (b) Phase 2 and (c) Phase 3. The dashed line shows the area where tensile angle ≈ 20° was seen.

The red color in Figure 5 indicates positive tensile angle, which can be derived from in-flow into fractures of rocks and the green color indicates negative tensile angle by out-flow. The angle of seismic events in Phase 1 shows smaller value (~ ±5°) compared to those in Phase 2 and Phase 3, in which large tensile angles (~ 20°) were observed. Especially in Phase 2, the large tensile angles, which indicate in-flow, distribute around the Test Well and the existing fault, where Mqs 2 was created. In Phase 3, large tensile angles were also observed near Mqs 3.

5. DISCUSSION

Okamoto et al. (2018) pointed out that a structure having high-impedance contrast (e.g., fracture zone) may exist between the injection point and the existing fault area (Figure 6). They estimated the high-impedance structure by using a diffraction stack migration of scattered and reflected waves in S-codas. The result of the focal mechanism analysis indicates that the injected water could flow toward the existing fault area, where Mqs 2 was created, from the injection point possibly through the high-impedance structure. The high-impedance structure may have high permeability because the injected water could pass through the structure without seismicity. Okamoto et al. (2018) also mentioned that elastic wave velocities in rock pores around Mqs 2 were increased after the water injection by using a seismic scattering analysis. Their result may suggest that water vapor in the rock pores were replaced by liquid water derived from the injected water.

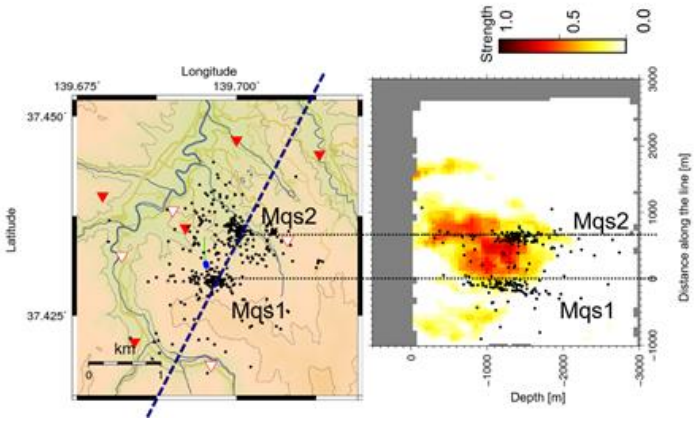

Figure 6: Distribution of microseismic events. (Left panel) Horizontal plot and (right panel) cross-section along the blue dashed line in the left panel. The contour shows the strength of S-wave reflectivity (Okamoto et al., 2018).

6. SUMARRY

We introduced a focal mechanism analysis using a genetic algorithm considering non-DC components to estimate water flow. We used polarity of P-waves and ratio of P- and S-wave amplitudes to construct the objective functions. The analysis revealed a water flow associated with the water injection test in the Okuaizu Geothermal Field. Microseismic monitoring can illuminate the water flow in the geothermal reservoir.

ACKNOWLEDGMENTS

This study was performed as a part of the “Technology to evaluate and manage geothermal reservoirs” sponsored by Japan Oil, Gas and Metals National Corporation (JOGMEC).

REFERENCES

Aki, K., Scaling low of seismic spectrum, *J. Geophys. Res.*, **72**, (1967), 1217-1231.

Baria, R., Baumgärtner, J., Gérard, A., Jung, R., and Garnish, J.: European HDR research program at Soultz-sous-Forêts (France) 1987-1996, *Geothermics*, **28**, (1999), 655–669.

Fehler M., House, L., and Kaieda, H., Determining planes along which earthquakes occur: Method and application to earthquakes accompanying hydraulic fracturing, *J. Geophys. Res.*, **92**, (1987), 9470–9414.

Kwiatek, G., and Ben-Zin, Y., Assessment of P and S wave energy radiated from very small shear - tensile seismic events in a deep South African mine, *J. Geophys. Res.*, **118**, (2013), 3630-3641.

Okabe, T., Kato, M., Sato, T., Abe, Y., Asanuma, H., Oishi, T., Tosha, T., Current status of the EGS project for water injection in the superheated region at Okuaizu Geothermal Field in Japan, *Proceedings*, 38th New Zealand Geothermal Workshop, Auckland (2016).

Okamoto, K., Yi, L., Asanuma, H., Okabe, T., Abe, Y., and Tsuzuki, M., Triggering processes of microseismic events associated with water injection in Okuaizu Geothermal Field, Japan, *Earth, Planets and Space*, **70**, (2018), doi: 10.1186/s40623-018-0787-7.

Ou, G.B., Seismological studies for tensile faults, *Terr. Atmos. Ocean. Sci.*, **19**, (2008), 463-471.

Schaff, D.P., Bokelmann, G.H.R., Ellsworth, W.L., Zanzerkia, E., Waldhauser, F., Beroza, G.C., Optimizing correlation techniques for improved earthquake location. *Bull Seism Soc Am.*, **94**, (2004), 705–721.

The New Energy Development Organization, Geothermal development promotion survey No. B-1 "Sarukuradake Area": Geothermal development research report, (1997), Available via http://geothermal.jogmec.go.jp/gathering/file/42.pdf. Accessed 11 Jan 2019

Vavryčuk V., Hrubcová P., Seismological evidence of fault weakening due to erosion by fluids from observations of intraplate earthquake swarms. *J. Geophys. Res.*, **122**, (2017), 3701-3718.

Waldhauser, F., Ellsworth, W.L., A double-difference earthquake location algorithm: Method and application to the Northern Hayward Fault, California, *Bull. Seism. Soc. Am.*, **90**, (2000), 1353–1368.